Research article

# NH₂-MXene/OXG nanocomposite hydrogel with efficient photothermal antibacterial activity for potentially removing biofilms

Yan Zhang [a,b,1], Hua Wei [d,1], Pingguang Zhu [a], Xiaojuan Hao [a,b,\*], Jing Chen [c,\*\*], Haina Zhang [a,\*\*\*]

[a] Joint Research Centre on Medicine, The Affiliated Xiangshan Hospital of Wenzhou Medical University, Ningbo, Zhejiang, 315799, China
[b] Zhejiang Engineering Research Center for Tissue Repair Materials, Wenzhou Institute, University of Chinese Academy of Sciences, Wenzhou, Zhejiang, 325000, China
[c] Institute of Medical Sciences, The Second Hospital and Shandong University Center for Orthopaedics, Cheeloo College of Medicine, Shandong University, Jinan, 250033, China
[d] Key Laboratory of Colloid and Interface Chemistry, Ministry of Education, School of Chemistry and Chemical Engineering, Shandong University, Jinan, 250100, China

## ARTICLE INFO

## ABSTRACT

The adhesion of bacteria to the surface leads to formation of biofilms causing numerous infection problems in implanting medical devices or interventional therapy. Traditional treatment for such problems is generally to administrate patients with antibiotics or antifungal agent. Alternatively, devices are taken out of the body to mechanically destroy the biofilm and re-used by surgery. In this study, a straightforward method was developed to remove biofilms using a MXene-based photothermal hydrogel. The hydrogel consists of dynamic crosslinking network formed by Schiff-base reaction between aldehyde-containing xyloglucan (OXG) and amine-containing MXene (NH₂-MXene), which showed efficient killing of both gram-positive *Staphylococcus aureus* (*S. aureus*) and gram-negative *Escherichia coli* (*E. coli*) bacteria upon near-infrared (NIR) laser irradiation. The NH₂-MXene/OXG nanocomposite hydrogel showed a high photothermal antibacterial efficiency and stable photothermal conversion, demonstrated by efficient removal of biofilms *ex vivo*.

## 1. Introduction

The infection caused by medical devices and implants is a major clinical complication [1], which costs \$5–10 billions annually worldwide for treatment. It prolongs the hospitalization time, thus increasing the burden of the hospitals and bringing clinical complications for patients [2]. In the process of implanting medical devices or interventional therapy, patients can suffer from

---

health-related infections because of bacterial adhesion to the surface of devices [3,4]. Generally, the specific invasive process includes a series of different events, including the adhesion, proliferation, migration of the planktonic bacteria, and finally the formation of bacteria biofilms [5]. The definitive treatment to eradicate infections once the biofilm has been established is generally local debridement by surgery and even thorough excision of the implant [6]. Currently, the common cleaning methods of biofilms include physical scraping [7], air powder abrasion [8], ultrasonic cleaning [9], and *in situ* electrochemical oxidation [10] of the explanted devices. However, these techniques may alter the surface properties [10], be difficult to clean the surface of complex shapes such as deep and narrow bone defects [11], require substantial treatment time, and yet only achieve partial removal of bacteria and surface contaminants, thus having limitation. Therefore, it is critical to develop an effective method to quickly destroy and completely remove biofilms in order to realize the *ex vivo* renovation of medical devices and implants during surgery. Photothermal therapy (PTT) is a potential solution to eliminate bacterial biofilms efficiently and quickly [12], which ensures the real aseptic safety and efficient bacteria removal during the renovation process of surgically removed medical devices and implants taken out from the body, and is becoming a major focus of related research.

Although PTT, which combines pulsed laser and strong light-absorbing materials, is a promising new method for bacteria disinfection, the practices of *in situ* administrating photo-triggered agents (usually small molecules) near the medical implants were impeded by nonspecific binding, aggregation, environmental instability, resistance after repeated uses, and systemic toxicity [13]. In contrast, nanomaterials show more effective and safe characteristics, for instance, the nanoeffect, large surface-to-volume ratio, and flexible surface modification that enable them to have increased bioavailability, improved biosafety, and enhanced therapeutic efficacy [14]. The combination of nanomaterials and PTT may be the most efficient antibacterial method.

Especially, 2D nanomaterials such as graphene and MXene have shown superior antibacterial properties with greatly reduced resistance under PTT. These 2D materials can absorb near inferred (NIR) resulting in high local heat by light irradiation. The combination of these 2D materials and PTT can potentially eliminate bacteria physically by heat that does not raise the concern of drug-resistance development commonly faced by antibiotics [15].

MXene generally exhibits metallic conductivity, high photothermal-conversion, and good hydrophilicity, making it a potential candidate as a highly effective PTT agent for antibacterial utilization [6,16–19] in medical treatment [20]. For instance, in Wu et al.'s [17] investigation, MXene shows significant antibacterial effects in 20 min under PTT (808 nm light). Another photothermal MXene-containing hydrogel showed efficient and rapid antibacterial activity under 808 nm light irradiation by loading the MXene in the cellulose-metal-organic hydrogel [21]. The monolayer high-entropy MXenes in Shen et al.'s [22] research is effective nanotherapeutic agent in the treatment of bacterial infections caused by methicillin-resistant *Staphylococcus aureus* (MRSA) (kill rate of 67.7 %), especially in synergistic use with the NIR-II enhanced endogenous oxidase, killing up to 96.5 % of the bacteria. However, it should be noted that MXene, similar to most nanomaterials, also suffers from aggregation in complex matrixes [23]. Usually, surface modification can improve the homogeneity of these nanosystems in aqueous media. (3-Aminopropyl)triethoxysilane (APTES) is commonly used to decorate MXene with functional groups like –NH$_2$ as NH$_2$-MXene to improve dispersibility and stability [24], thus promoting its wide applications [25,26].

Natural polysaccharides, by virtue of their sustainability, biocompatibility, abundance, and cost factors, have been widely studied and used in biomedical applications [27,28]. Xyloglucan (XG) is a main polysaccharide and interwoven cellulose microfibril existing in most flowering plants [29]. Because of intermolecular hydrogen bonding and chain entanglement, it has high adhesion and good film-forming ability [30]. Pure XG extracted from tamarind seed is difficult to beused as an aqueous solution [29], while water-soluble aldehyde-modified XG could be obtained by oxidation, and more importantly, the oxidized XG (OXG) even exceeds the performance of pristine XG in limited applications owing to the additional carbonyl clusters [27]. Herein, surface-modified MXene nanosheets (NH$_2$-MXene) and OXG were simply mixed to directly prepare a nanocomposite NH$_2$-MXene/OXG hydrogel. In the trials of bacterial biofilm clearance, the prepared nanocomposite hydrogel could sensitize bacteria toward hyperthermia and kill bacteria with NIR-responsive thermotherapy. In addition, such a hydrogel can be easily cleaned off without affecting the surface property of implant after removing biofilms due to its intrinsic self-healing property. The prepared binary adhesive hydrogel composed of dynamic Schiff-base crosslinked networks of OXG and NH$_2$-MXene. NH$_2$-MXene plays a dual role as a bactericide, i.e. photothermal conversion for sterilization and a component of Schiff-base reaction to participate in the construction of the hydrogel. OXG endows hydrogel certain adhesion and mechanical properties via participating in Schiff-base reaction with NH$_2$-MXene. Compared to other hydrogel systems [31], this hydrogel has the advantages of easy preparation, efficient and quick removal of biofilms (within 10 min), non-use of any antibacterial agents and thus no potential drug-resistance development, preferable use for efficiently cleaning explanted medical devices and implants *ex vivo*, but also possible use *in vivo* by injection as NIR can penetrate deep tissue to trigger the hydrogel generating a local heat. Therefore, the crosslink formation of amine and aldehyde groups between NH$_2$-MXene and OXG could steadily result in reversible nano filler hydrogels with good self-healing and bactericidal capacities, potentially useful for cleaning the biofilms on medical devices and implants by PTT [32].

## 2. Materials and methods

### 2.1. Materials

MXene Ti$_3$C$_2$T$_x$ (99.9 %) dispersion was purchased from Xinxi Technology Co, Ltd. (Foshan, China). (3-Aminopropyl)triethoxysilane (APTES) was procured from Sigma Aldrich, USA. Sodium periodate (≥99 %) was supplied by Titan Scientific CO, Ltd. (Shanghai, China). Tamarind gum was obtained from TCI Shanghai. Acetic acid (AR), sulfuric acid (GR, 95.0–98.0 %), ethanol (AR, ≥99.7 %), and hydrochloric acid (AR, 36.0–38.0 %) were provided by Hushi (Shanghai, China). Sodium hydroxide (≥97 %),

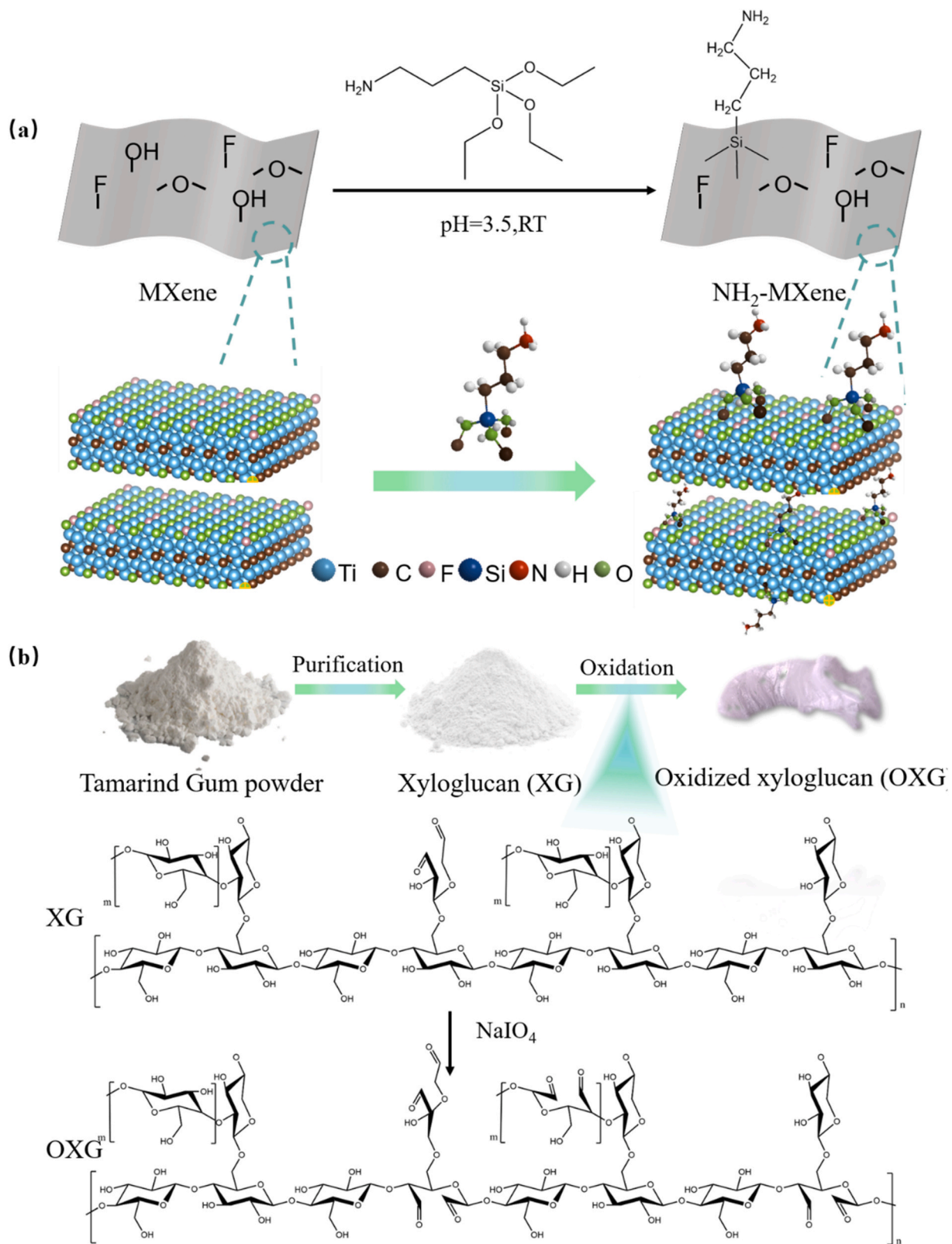**Fig. 1.** Graphical schemes for preparation of (a) NH$_2$-MXene and (b) OXG.

hydroxylamine hydrochloride (AR, 98.5 %), and methyl orange were purchased from Aladdin (Shanghai, China). Deionized water was used during the course of the entire experiment.

## 2.2. Methods

### 2.2.1. Functionalization of MXene

APTES was used to modify the ultrathin $Ti_3C_2$-MXene nanosheets with an amine terminal as shown schematically in Fig. 1a [33]. Surface functionalization of MXene was carried out in a water/ethanol mixture (10/90 wt%) in order to provide enough amount of water for APTES hydrolysis reaction [34]. Initially, acetic acid was added to reduce pH of the aqueous MXene suspension to 3.5. Subsequently, APTES was completely dissolved in ethanol and the solution was added dropwise to the MXene suspension and agitated at room temperature under nitrogen bubbles for 8 h [35]. When the reaction was completed, the suspension was washed three times with ethanol by centrifugation to remove unreacted silane coupling agent from $NH_2$-MXene nanosheets. The final suspension was vacuum-filtered through polypropylene membranes and the obtained free-standing films were then dried in a vacuum oven at 60 °C for 24 h. The above films were put into a quartz mortar and soiled to get final $NH_2$-MXene powder.

### 2.2.2. Synthesis of oxidized xyloglucan

Xyloglucan (XG) was extracted from Tamarind Gum powder [29], which was firstly dissolved in deionized water to form homogeneous slurry, then the slurry was heated at 40 °C for 24 h, followed by centrifugation. This step was repeated three times to obtain its supernatant. Subsequently, the collected solution was cooled down and a fibrous precipitate was formed by the addition of ethanol, which was filtered and freeze-dried. Freeze-dried material referred as XG was stored in an airtight container for use.

The oxidation reaction of XG was carried out in an aqueous solution by using periodate as oxidizing agent as shown schematically in Fig. 1b. The ratio of sodium periodate to XG was 1:10. In detail, The XG was solubilized in distilled water, followed by the addition of an aqueous solution of sodium periodate under stirring. The reaction was kept for 2 h with magnetic stirring in the dark at 25 °C. After 2 h, the reaction was quenched by addition of ethylene glycol. The oxidized XG (OXG) was purified by dialysis against distilled water for 2 days and the resulting product was freeze-dried [30].

### 2.2.3. Fabrication of $NH_2$-MXene/OXG hydrogel

First, OXG solution (1.5 wt%) was obtained by dissolving OXG in deionized water at room temperature under magnetic stirring for 12 h until a homogeneous solution was obtained. A required amount of $NH_2$-MXene nanosheets prepared into solutions of different concentrations by sonicating was mixed with OXG solution to form precursor solutions of $NH_2$-MXene/OXG with different molar ratio. The mixture was stirred for 1 h to uniformly disperse the $NH_2$-MXene nanosheets in the precursor solution [20], in which $NH_2$-MXene and $NH_2$-MXene/OXG eventually form a hydrogel.

### 2.2.4. General characterization

An 808 nm laser was used as the NIR light source and the thermography was collected through a thermal camera (FLIR E8-XT, USA). The chemical bonds of MXene, $NH_2$-MXene, raw material XG, and OXG were analyzed by Fourier transform infrared (FTIR) spectrometer (Thermo Fisher Nicolet Nicolet 6700 FTIR Spectrometer, USA) in attenuated total reflectance (ATR) mode. Chemical composition and crystalline structure of MXene and $NH_2$-MXene were identified by X-ray photoelectron spectroscopy (XPS) (Kratos, Axis Ultra DLD, UK) and XRD (Bruker, D8 ADVANCE, Cu Kα, 2θ scan range of 3°–70°), respectively. Furthermore, TEM images were acquired with the Talos F200x transmission electron microscope. The thickness of MXene and $NH_2$-MXene flakes was measured through atomic force microscope (AFM, Bruker, Dimension FastScan). Thermogravimetric analysis (TGA) was carried out on the pristine MXene and $NH_2$-MXene powders using STA 449F3 TG-DSC (Netzsch, Germany), which was conducted from room temperature to 800 °C with a heating rate of 10 °C/min under a flowing nitrogen atmosphere under vacuum.

A pH meter (F2-Field Kit, mettler toledo) was used to monitor the change of pH value in the process of titration of amine and aldehyde groups. The amine group content in the $NH_2$-MXene was calculated by adding the NaOH solution to the HCl/$NH_2$-MXene mixture. Similarly, the content of aldehyde group was determined by potentiometric titration with hydroxylamine hydrochloride. Firstly, the OXG was dissolved in hydroxylamine hydrochloride to form a homogeneous solution, and then the amount of $H^+$ in HCl is titrated by potentiometric titration with NaOH to obtain the specific degree of modification.

The pore structure and element distribution of $NH_2$-MXene/OXG hydrogels were characterized by scanning electron microscope (SEM) (Regulus 8230, Hitachi, Japan). Rheological properties of freshly prepared mixture were measured using a Discovery HR-2 (TA Instrument, USA) equipped with a temperature sensor and a 25 mm plate geometry at 25 °C. Amplitude measurements were firstly performed to confirm the data fall within the linear viscoelastic strain region. In the frequency range of 0.1–100 rad/s, dynamic frequency scanning was performed with 10 % constant stress in the linear region. In order to characterize the temperature dependence and self-healing properties of hydrogels, the changes of hydrogel modulus under cyclic shear at high (2000 %) and low (10 %) strains were monitored. The lap shear adhesion tests of hydrogel samples were carried out by universal testing machine (CMT-1104, SUST). All hydrogel samples were fixed as standard rectangular samples with a length of 20 mm, a width of 15 mm, and a thickness of 1 mm.

Hydrogel discs of $NH_2$-MXene/OXG with different composition were added to bacterial solutions ($10^6$ Colony-Forming Units (CFU)/mL) in the well plate and irradiated with or without 808 nm light. After treatment, the above-mentioned orifice plate was placed on shaking incubator for 4 h at 100 rpm and 37 °C. Then the bacterial suspension of each group was diluted 100 folds, and 100 μL of the dilutions was dropped onto Luria-Bertani/Tryptone Soy Broth (LB/TSB) plates to grow for 12–24 h at 37 °C.

### 2.2.5. SEM and confocal laser scanning microscopy of live and dead bacteria in biofilms

The polished and sterilized titanium plate was placed in the bacterial solutions ($10^8$ CFU/mL) and incubated for 24 h at 37 °C to form mature biofilms. Then, different NH$_2$-MXene/OXG hydrogel discs were put on the surface of Ti biofilm, and illumination was applied. After that, the hydrogels were removed, and the surface of the titantium plates were gently washed with sterile PBS buffer solution for three times to remove planktonic bacteria. Then the formed biofilms were stained with a live/dead bacterial viability kit (Invitrogen) for 15 min, washed twice with sterile water, and then imaged by confocal laser scanning microscope. The flat plate with biofilm was uniformly dyed with 4 % paraformaldehyde, and dehydrated by 25 %, 50 %, 75 %, and 100 % ethanol for 10 min in order to observe the biofilm under SEM.

### 2.2.6. Statistical analysis

Data processing was conducted using Microsoft Excel (Microsoft®, USA). The results were expressed as a mean ± standard error of the mean for each sample. Each experiment was repeated independently three times. A two-sided T-test was used to compare the data, assuming equal variances. Data were expressed as average (±SD); 0.05 was chosen as the signiffcance level, and (*) for $p < 0.05$, (**) for $p < 0.01$, and (***) for $p < 0.001$, respectively.

## 3. Results and discussion

### 3.1. Characterization of pristine and functionalized materials

In order to confirm the existence of amine groups on the surface of NH$_2$-MXene, FTIR was used to analyze the changes in the surface chemical states before and after the functionalization of MXene samples [36]. It is well known that triethoxyl groups of silanes first hydrolyze into trihydroxyl groups, then, condensation of the hydroxyl groups between silanols and the surface of the MXene occurred, resulting in NH$_2$-MXene [24]. As shown in Fig. 2a, the characteristic peak at around 3200 cm$^{-1}$ was observed from the functionalized MXene, which corresponds to –NH$_2$ stretching vibration [37]. The residue –OH groups on the MXene surface show a shoulder peak next to –NH$_2$ peak at around 3300 cm$^{-1}$, overlapping with –NH$_2$ peak. Other evidences include the band at around 2920 cm$^{-1}$ showing the
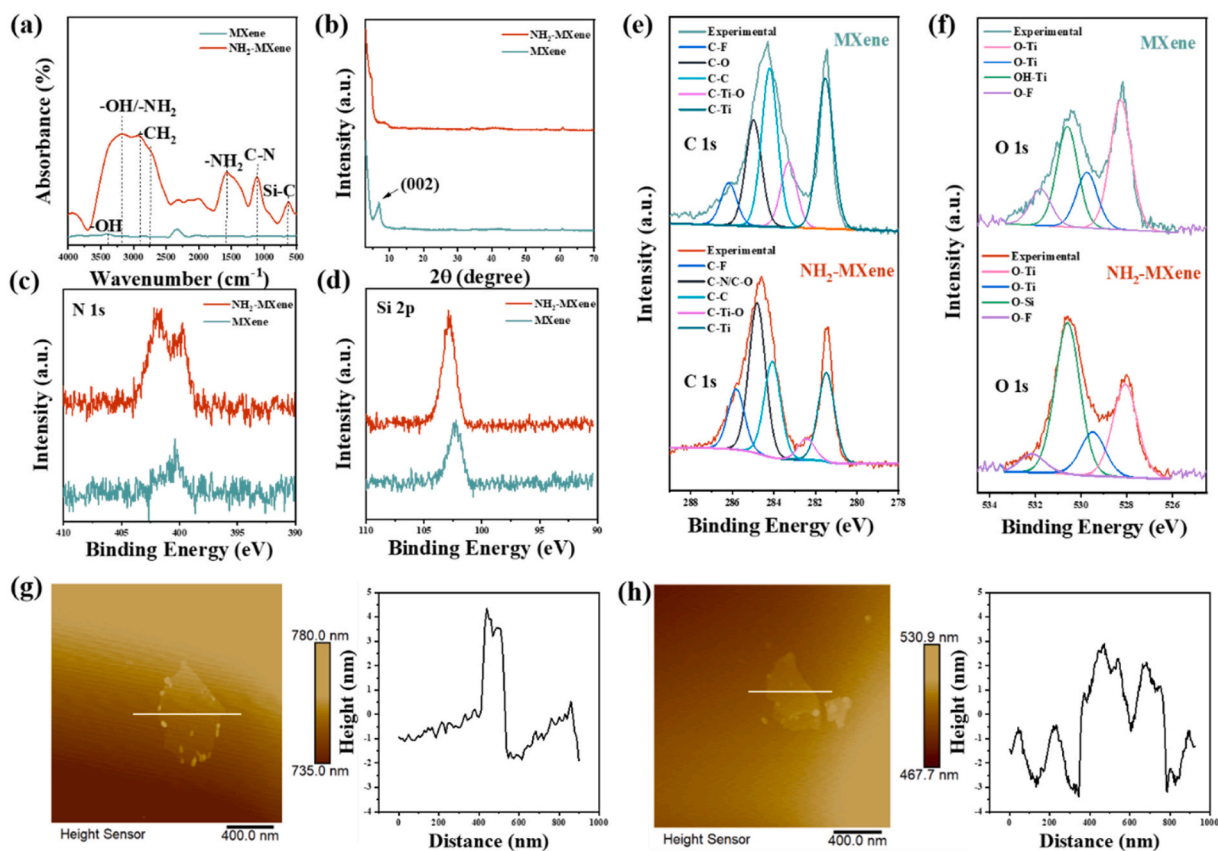


**Fig. 2.** (a) FTIR spectra of the pristine MXene and NH$_2$-MXene. (b) XRD patterns of MXene and NH$_2$-MXene nanosheets. X-ray photoelectron spectra of MXene and NH$_2$-MXene (c) N 1s spectra, (d) Si 2p spectra, (e) C 1s spectra, (f) O 1s spectra. AFM images and the thickness of (g) MXene nanosheets and (h) NH$_2$-MXene nanosheets.

existence of the $CH_2$ of APTES and a new peak at around 1535 cm$^{-1}$ attributed to $-NH_2$ scissor vibration in the $NH_2$-MXene [38]. In addition, the representative absorption peak at 1190 cm$^{-1}$ is related to the C–N stretch vibrations [39]. Therefore, it could be preliminarily proven that the primary amine groups were successfully introduced on the surface of MXene.

To in-depth verify the surface modification of MXene, XRD (Fig. 2b) was conducted to detect the change of crystal structure of the pristine and modified MXene. It could be observed that the diffraction peak intensity of $NH_2$-MXene decreases, which is due to the decrease of crystallinity. Furthermore, in comparison to MXene, the XRD peak (002) of $NH_2$-MXene shifts to a lower angle, which is indicative of enlarged interlayer spacing [40], resulting in decreased thickness of $NH_2$-MXene nano layers [33]. In order to further confirm the existence of amine groups on the surface of the $NH_2$-MXene, the atomic binding of XPS was obtained (Fig. 2c–f). With the functionalization of APTES for preparing $NH_2$-MXene nanosheets, spectra of N 1s (Fig. 2c) and Si 2p (Fig. 2d) showed increased intensity of corresponding peaks, which confirms that the MXene nanosheets had been successfully modified [38]. However, the unmodified samples also showed weak N and Si peaks, which could be attributed to the impurities in the experiment. The fitted C 1s spectra of the MXene and $NH_2$-MXene nanosheets are shown in Fig. 2e, in which C 1s peaks at 281 eV and 283 eV correspond to internal C–Ti bond and surface terminated C–Ti bond (C–Ti– O/F), respectively. The other peaks can be assigned to graphitic C–C (284 eV) and C–O (285 eV) bonds. The weak peaks at high binding energy (286 eV) correspond to the C–F/O–C=O groups. However, after functionalization, the peak intensity of inner C–Ti layer decreases, and a strong peak for C–N is observed at about 285 eV, which indicates that there are APTES molecules on the MXene. Fig. 2f shows the O 1s spectra of pristine and modified MXene, in which four peaks of 528.2, 530, 531, and 532 eV can be attributed to O–Ti (corresponds to oxygen bonded to surface titanium), O–Ti (corresponds to oxygen bonded to titanium incorporated into bulk Mxene), OH–Ti, and O–F bonds in the pristine MXene. The detailed information about $NH_2$-MXene includes O–Ti (528.1 eV), O–Ti (529.5 eV), O–Si (530.8 eV), and O–F (532.1 eV), respectively. These results further confirm the formation of amine-functionalized MXene [36].

Figure S 1a shows TGA curves of the pristine and modified MXene under a nitrogen atmosphere, in which pristine MXene shows two step changes in mass loss. The first mass loss from 25 to 100 °C corresponds to the dehydration of the interlayer water, while the second mass loss from 100 to 800 °C is related to the decomposition of terminated groups, resulting in the generation of $CO_2$ along with the transformation of the scaffold into titanium carbide (TiC) [39]. In comparison, the first mass loss of $NH_2$-MXene also corresponds to the desorption of water. The second mass loss occurred between 100 and 220 °C, revealing the release of methane and amine anion, which is in agreement with the decomposition of physiosorbed APTES [34]. The sharp drop from 220 °C to 430 °C involves the release of methane, $NH_3$, $NH_2$, and $N_2$ from embedded APTES in MXene layers. The electrostatic interaction between $NH_3^+$ of APTES and –OH surface termination groups of the MXene requires more energy to decompose [39]. The remaining masses of $NH_2$-MXene are approximately 97.18 %, 93.70 %, and 85.69 % in three different stages, respectively [41], which are lower than that of pristine MXene (98.59 %, 97.65 %, and 96.31 %, respectively). This indicates that the weight percentage of grafting groups is 6.67 % [40]. There are also other methods to determine the amine group content, such as potentiometric titration, which can improve the quantification accuracy. As shown in Fig. S 1b, the modification degree of the amine group was calculated as 5.2 mmol/g.

The morphology and the elemental distribution of MXene and $NH_2$-MXene were characterized by TEM. Both MXene (Fig. S 1c) and $NH_2$-MXene (Fig. S 1d) nanosheets exhibit very thin, highly transparent and smooth surface, which proves that functionalization would not affect the morphology of the MXene. $NH_2$-MXene sheet looks more gauzy (Fig. S 1d), which may be because APTES was grafted onto the MXene layers and the steric hindrance effect prevented the aggregation of MXene nanosheets [25]. Furthermore, due to the shearing forces applied from the stirring process, the size of the sheets is reduced [38]. AFM measurements confirm that the thickness of the MXene nanosheets was reduced by the modification. The AFM images of the MXene and $NH_2$-MXene are shown in Fig. 2g and h. The thickness of the MXene is about 4 nm and the average thickness of $NH_2$-MXene is about 3 nm, indicating the formation of $NH_2$-MXene and also implying that the $NH_2$-MXene possesses less aggregated structures.

The oxidation of XG causes the rupture of carbon–carbon bond and the two aldehyde groups are formed in each oxidized monomeric unit [29,30]. The oxidation of XG using $NaIO_4$ was analyzed by FTIR (Fig. S 2a), in which the peak at around 1730 cm$^{-1}$ assigned to C=O stretching becomes stronger for OXG. In addition, the aldehyde content in oxidized samples can be accurately determined by potentiometric titration of hydroxylamine hydrochloride. The specific principle is shown in Fig. S 2b, c, and the modification degree of the aldehyde group was calculated as 0.6 mmol/g.

## 3.2. Characterization of binary $NH_2$-MXene/OXG nanocomposite hydrogel

### 3.2.1. Rheological properties of precursors

Dynamic mechanical analysis of the precursors provides quantitative information about viscoelastic and rheological properties of the materials by measuring the mechanical response of the samples when they are deformed under periodic strain. The elastic (storage) modulus G′ and the viscous (loss) modulus G″ are presented [42]. Most polysaccharide gels are reversible physical gels formed by hydrogen bonding, electrostatic interaction, hydrophobic interaction, and van der Waals force, etc. The structure and shape of polysaccharide molecules, molecular weight and molecular weight distribution, intermolecular interactions, and temperature are the key factors affecting its flow behavior [43]. XG has a unique branched structure, which makes it highly viscous in water [30]. It was also reported that xyloglucan alone can form a gel if a part of the galactose is removed [29,44]. In this study, sodium periodate was used to oxidize the side chain galactose of XG to obtain aldehyde groups. It can be inferred that OXG induced drastic self-assembly transition [44], which unusually makes the storage modulus rheologically larger than the loss modulus of the OXG solution (G'>G″), although the OXG solution is liquid-like. In contrast, the storage modulus of $NH_2$-MXene solution in Fig. S 3b is always lower than the loss modulus, indicating that $NH_2$-MXene alone presents typical solution properties, consistent with actual observation.

The rheological analysis of the mixed precursor solutions with different $NH_2$-MXene/OXG ratios was presented by the results of the

G′ and G″ vs time. It was observed that when NH$_2$-MXene/OXG molar ratio in aqueous solution was 1:1 and 2:1 (Fig. S 3c, d), the behavior of the mixed solutions is very similar to the typical characteristics of OXG solution, indicating that OXG dominates the property. There is no obvious change in storage modulus, which proves that the mixed solution has no strong network structure, but the doping of nanosheets increases viscosity because of hydrogen bonding, that is, the loss modulus increases.

According to the results of Fig. S 3e, f, it was observed that when NH$_2$-MXene/OXG molar ratio in aqueous solution increases to 3:1 and 4:1, the starting loss modulus of the mixed solution increases to 1 Pa, and both storage modulus and loss modulus tend to increase with time. In addition, a G′ and G″ crossover point was observed with 4:1 hydrogel, which indicated that a three-dimensional network structure was formed via hydrogen bonding and Schiff-base crosslinking [45].

When the molar ratio of NH$_2$-MXene to OXG reaches 5:1, the storage modulus and loss modulus of the hydrogel both increase with mixing time (Fig. S 3g), and a clear crossover point was also observed with the final storage modulus reached around 100 Pa, much higher than 4:1 hydrogel, indicating the formation of a stronger hydrogel. Additionally, the SEM image of the hydrogel shows a clear and uniform network structure (Fig. 3). These findings further confirm the network formation of the hydrogel via Schiff-base bond and hydrogen bonding. The advantage of this kind of binary nano filled hydrogel based on Schiff-base crosslinking is its self-healing property. In the actual applications, traditional hydrogels are prone to damage, resulting in broken residues, which are difficult to clean. Self-healing properties of the hydrogel can potentially address this challenge. In order to verify the self-healing behavior of the hydrogel, the multi-step strain oscillation measurements were carried out, in which the frequency was kept at 10 rad/s and the strain was changed alternately at low (10 %) and high (2000 %) [46]. As shown in Fig. S 3h, after the first cycle of 10%–2000 % strain change the 5:1 hydrogel exhibited regular and repeatable modulus recovery phenomenon, which shows a typical self-healing behavior. However, a significant loss in G′ of the hydrogel from the first cycle to the second cycle was observed, which can be attributed to the high strain extrusion in the second cycle, and the incomplete recovery of the hydrogel modulus in the subsequent low strain test (10 %) can be attributed to the reduction of the number of recombinant hydrogen bonds [47]. In practical biomedical applications, such efficient and reproducible self-healing property is highly preferred.

Furthermore, there is no obvious modulus change of the hydrogel with change of temperature, so it can be understood that the state of the hydrogel does not change significantly during the photothermal process and the structure is stable during cyclic heating and cooling (Fig. S 3i).

### 3.2.2. Morphology investigation of binary nano hydrogel

The introduction of NH$_2$-MXene nanosheets plays an important crosslinking role in improving the mechanical strength of the hydrogel network [18], which has been studied by rheology discussed above. The SEM results show that the nano-crosslinking based on Schiff-base reaction forms a complete network, thus producing a harder hydrogel that can bear mechanical load. The 5:1 hydrogel (Fig. 3) showed large uniform pores, and the corresponding EDS elemental map showed that the elements C, O, Ti, N, Si are uniformly distributed in the hydrogel, indicating that NH$_2$-MXene nanosheets are uniformly dispersed in the hydrogel as well [48]. This further confirms the successful preparation of hybrid NH$_2$-MXene/OXG nanocomposite hydrogel.

### 3.2.3. Photothermal effect and stability of NH$_2$-MXene/OXG nanocomposite hydrogel

Photothermal activity was conducted using a NIR laser (808 nm), and thermogram of the 5:1 NH$_2$-MXene/OXG nanocomposite hydrogel is shown in Fig. 4a. Different power and time were used for NIR radiation. The photothermal heating experimental results of the hydrogels are shown in Fig. 4 (5:1 ratio) and Fig. S4 (3:1 and 4:1 ratios), respectively, which show that the hydrogels have similar photothermal activity as original MXene (Fig. S 4a-1). The photothermal-conversion efficiency of the hydrogels is dependent on light intensity and exposure time under NIR laser irradiation, as shown in Fig. 4b and Fig. S 4a-2, b-2, c-2. Upon 808 nm light irradiation,
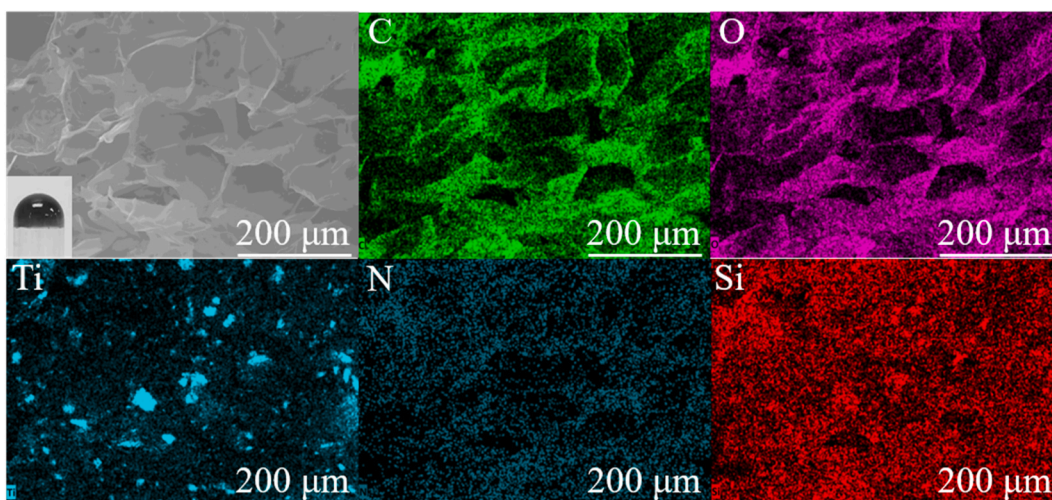


**Fig. 3.** SEM images of the network structure of binary 5:1 NH$_2$-MXene/OXG hydrogel and the distribution of C, O, Ti, N, Si elements.

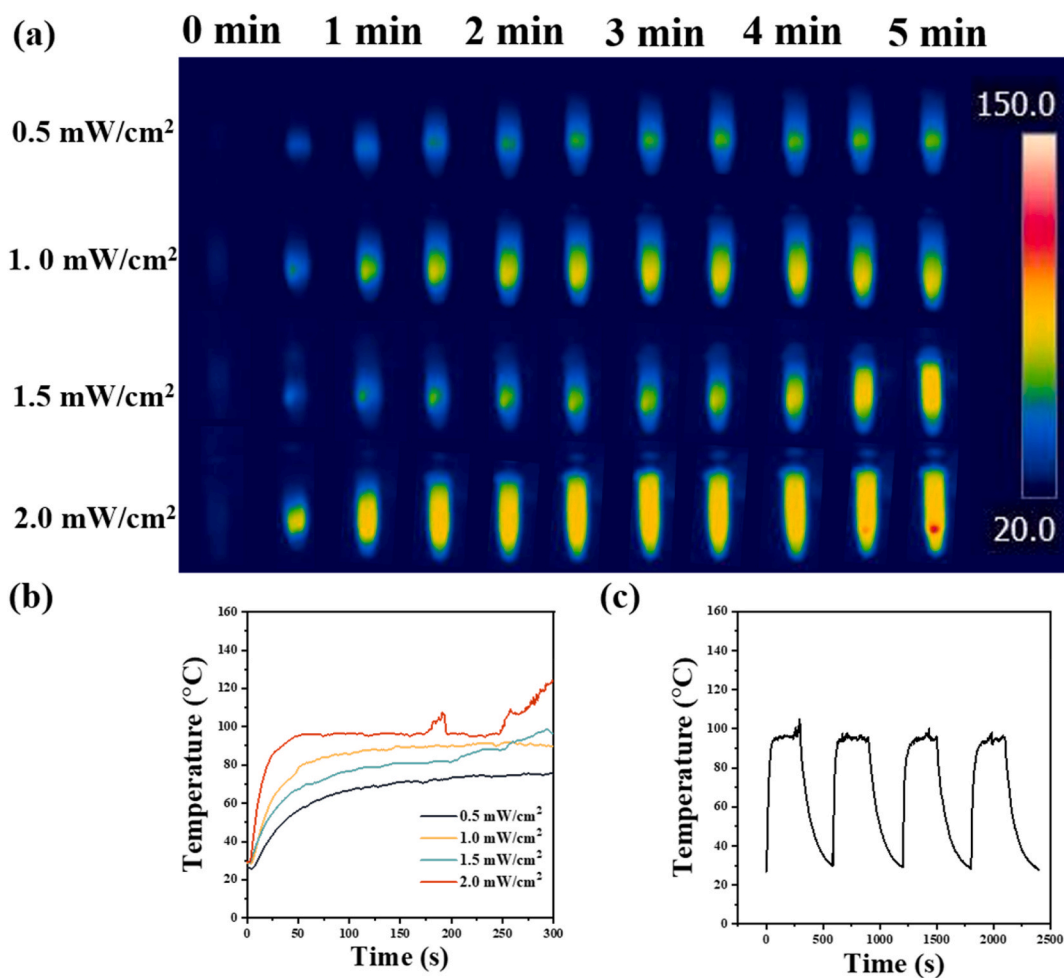**Fig. 4.** (a) Photothermal heating images of $NH_2$-MXene/OXG nanocomposite hydrogel under 808 nm NIR irradiation at different power up to 5 min of 5:1 hydrogel. (b) Photothermal heating curves of $NH_2$-MXene/OXG nanocomposite hydrogel under 808 nm NIR irradiation at different power for 5 min of 5:1 hydrogel. (c) Photothermal stability cycling test of $NH_2$-MXene/OXG nanocomposite hydrogel of 5:1.

both pristine MXene nanosheets and binary nanocomposite hydrogels showed a significant temperature rise within 50 s under different irradiation power, indicating a high photothermal-conversion efficiency. Increasing the exposure time after 50 s no longer changes temperature. The increase of the $NH_2$-MXene nanosheets content in the hydrogel seems to improve the photothermal properties, more importantly, increases the mechanical properties as well. Also, the light intensity significantly influences photothermal-conversion efficiency. All the hydrogels show a stable temperature rise of above 90 °C within tested timeframe (5 min). In addition, in order to further study the laser-induced photothermal stability of hybrid hydrogels, cyclic temperature change was performed by repeated NIR laser irradiation on the hydrogels. The photothermal performance of pristine MXene did not perform apparent deterioration during four laser on/off cycles (Fig. S 4a-3), highlighting the superb photothermal performance of MXene [13]. Fig. 4c presents photothermal performance of the 5:1 hydrogel under the lay and remove of 808 nm light and the specific results show that this hydrogel has a higher stability close to pristine MXene, compared to other hydrogels (3:1 and 4:1, Fig. S 4b-3, c-3).

For the current work, it is enough to point out that the heating rate increases obviously with the increase of the $NH_2$-MXene content, as well as the NIR irradiation power. Therefore, the 5:1 hydrogel shows an excellent photothermal activity, potentially leading to excellent antibacterial performance. For comparison, the pure OXG solution shows no heating effect under NIR irradiation as shown in Figure S 5a.

### 3.2.4. Adhesive property of binary nano hydrogel

Adhesive strength is a basic measure of mechanical properties of adhesives, which is usually obtained by lap shear tests. A general procedure of lap shear test to assess the ability of an adhesive to withstand stress is shown in Fig. S 5b, where two parallel plates are joined together by an adhesive (here the adhesive is a hydrogel) and shear forces apply [49]. The prepared hydrogel showed the property of adhesion as shown in Fig. S 5c, which clearly shows that the higher the concentration of $NH_2$-MXene nanosheets in the hydrogel, the stronger the adhesive force. With this adhesive property, the hydrogel could be easily adhered to the surfaces of medical

devices and implants, and could also be easily removed through its self-healing property. The slight adhesive strength of the hydrogel can be attributed to the presence of abundant amine and hydroxyl groups as well as physical entanglements and interlocking property of the binary hydrogel [49].

### 3.3. Antibacterial assays

The significant photothermal activity of the binary NH$_2$-MXene/OXG nanocomposite hydrogel enlightened us to evaluate its antimicrobial performance. Photothermal antimicrobial ability of the 5:1 hydrogel towards *S. aureus* and *E. coli* was studied. These two kinds of bacteria were selected as representatives for Gram-positive and Gram-negative bacteria. The antibacterial efficiency was evaluated by measuring the cell viability using CFU counts. As shown in Fig. 5a and b, the culture images of bacterial colonies show that the hydrogel has remarkable antibacterial activity in combination with NIR irradiation (5 min, 2.0 mW/cm$^2$). Under the synergistic effect of 5:1 hydrogel and NIR, the highest death rates of *S. aureus* and *E. coli* were over 99 % and 70 %, respectively. The difference in the highest death rates of *S. aureus* and *E. coli* could be attributed to the sensitivity of two types of bacteria towards the temperature, with *S. aureus* more sensitive to the heat generated by the nanocomposite hydrogel and NIR irradiation [50].

The hydrogel experimental groups and the control group were treated with same procedure, i.e. exposed to NIR for 5 min and incubated for 4 h. In comparison of the representative photos of bacteria, the NIR light itself showed a slight antibacterial effect, possibly due to the heat generated by light irradiation. Additionally, the results indicated a dose-dependent antimicrobial activity of NH$_2$-MXene, showing that the NH$_2$-MXene/OXG hydrogel with a higher content of NH$_2$-MXene had a greater antibacterial effect on planktonic bacteria. In addition, the results also provided a surprising discovery, that is, the NH$_2$-MXene/OXG hydrogel showed a slight antibacterial activity alone without NIR irradiation. This can be explained by the inherent physical characteristics of MXene nanosheets, which have sharp edges and huge basal surfaces leading to inherent antimicrobial activity of the nanocomposite hydrogels mainly through physical interactions [15]. The bactericidal efficiency of hybrid hydrogel was much higher in combination with NIR irradiation.

Because it is difficult for antibiotics to penetrate the matrix of biofilm [17], it is hard to remove the mature and established biofilm adhered and deposited on the surface [51], and common mechanical biofilm repture only realizes partial bacteria removal [11]. In order to explore whether the prepared nanocomposite hydrogel could eliminate bacteria in biofilm in combination with light, we grew biofilm on the surface of a titanium plate mimicking a medical device, and then exposed the biofilm to NH$_2$-MXenes/OXG hydrogel,
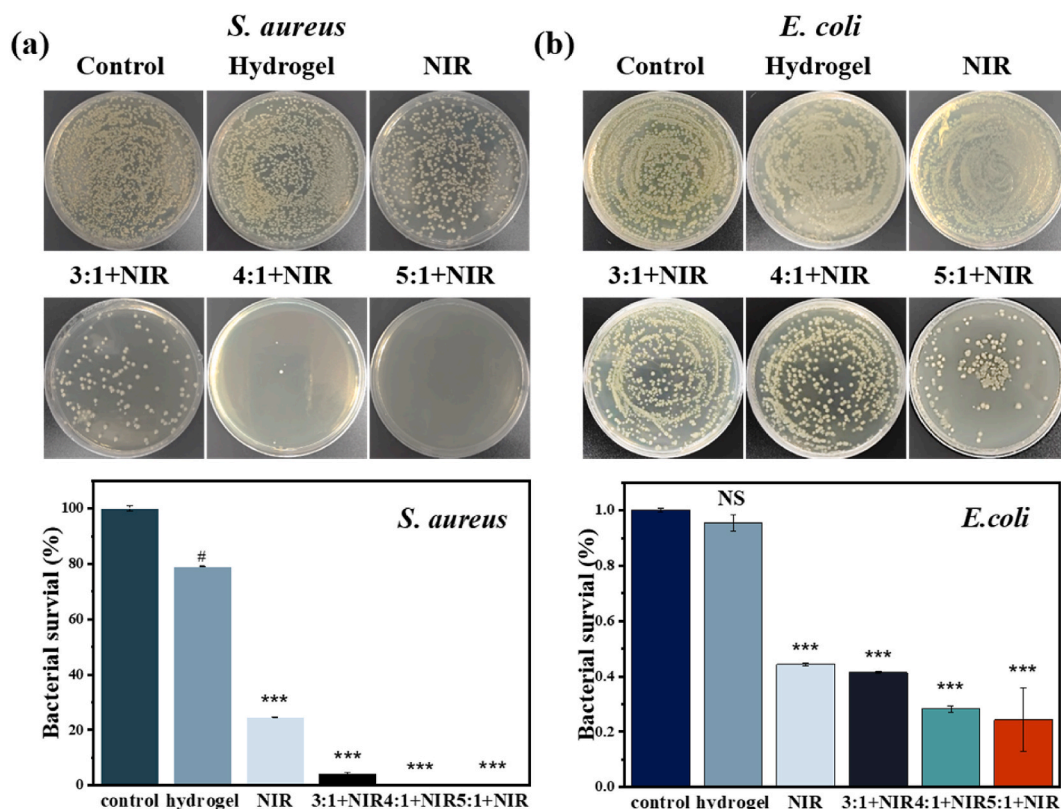


**Fig. 5.** Representative culture images and mathematical statistics chart of bacterial colonies from (a) *S. aureus* and (b) *E. coli* after no exposure (control), exposure to 5:1 hydrogel alone, exposure to light (2.0 mW/cm$^2$) alone, and simultaneous exposure to hydrogel (3:1, 4:1, and 5:1) and light (2.0 mW/cm$^2$) for 5 min. Data shown as mean ± SD. N = 3 per group. vs Control, #$p < 0.05$, ***$p < 0.001$.

followed by irradiation of 808 nm light (2.0 mW/cm$^2$) for 5 min. SEM images (Fig. 6a and b) showed that the control group was covered by live bacteria with a dense stacking biofilm structure. The biofilm placed in contact with the hydrogel alone still had a complete structure, and a similar survival rate to the biofilm exposed to NIR alone (in one PTT cycle) or slightly reduced survival rate compared with the control. In contrast, the biofilms were significantly damaged and nearly no live bacteria in biofilm could be found in 5:1 hydrogel group under NIR irradiation. Accordingly, the NH$_2$-MXene/OXG hydrogel combined with NIR irradiation can be introduced as an antibacterial method, which not only inhibits the formation of mature biofilm but also induces bacterial apoptosis. In order to further explore the antibacterial effect of nanocomposite hydrogel on biofilm treatment under NIR irradiation, the biofilm was exposed to two cycles of radiation in hybrid hydrogels with different concentrations of NH$_2$-MXene nanosheets. Compared with other groups, the survival rate of bacteria in biofilm exposed to 5:1 hydrogel for two rounds of NIR radiation was greatly reduced. These results showed that the combination of NH$_2$-MXene/OXG hydrogel and light could not only kill bacteria in biofilm, but also destroy the structure of biofilm, so it shows a fast and effective biofilm removal strategy.

The antibacterial effect was further confirmed by the live/dead staining results displayed by the laser confocal microscope images (Fig. 7a and b). It could be seen that the red fluorescence was higher in the groups of hydrogels under NIR light where green fluorescence represented live bacteria and red fluorescence represented dead bacteria. In particular, the intensity of red fluorescence is the highest with 5:1 NH$_2$-MXene/OXG hydrogel, representing the best antibacterial performance compared to other groups, attributed to its strong photothermal property. The results also showed that the hydrogel alone had a slight antibacterial effect, which is due to the direct physical interactions between the sharp edges of the nanosheet and the surface of the bacteria membrane [13]. Likely, the antibacterial performance of the hydrogel against *E. coli* under NIR light is worse than that of *S. aureus*. In addition, no matter whether the bacteria are in floating state or biofilm state, the hybrid NH$_2$-MXene/OXG nanocomposite hydrogel with NIR light has the advantage that drug resistance is unlikely to occur, because the antibacterial mechanism is mainly physical damage through photothermal effect.

## 4. Conclusion

MXene nanosheets were functionalized by APTES and successfully fabricated into NH$_2$-MXene/OXG nanocomposite hydrogel via Schiff-base reaction with OXG. The obtained hydrogel showed the characteristics of self-healing, adhesion, and antibacterial effect with PTT. The bactericidal mechanism of the hydrogel against planktonic bacteria and biofilm was investigated, showing synergistic antibacterial effects under the irradiation of NIR. Specifically, the NH$_2$-MXene/OXG nanocomposite hydrogel at the molar ratio of 5:1 showed extraordinary photothermal property and could efficiently damage the cell wall of bacteria via a rapid temperature rise. Therefore, this kind of hydrogel provides a potential method for cleaning the bacterial biofilms on the medical devices and implants to renovate them. In the course of removing *E. coli* planktonic bacteria and biofilms, the prepared hydrogel showed a lower efficacy (over 70 %) compared to *S. aureus* bacteria (over 99 %). Therefore, in the future work, to further improve the efficacy of removing *E. coli* biofilms the hydrogel could be used in combination with an antibacterial agent to make sure a complete removal achieved. Although the present work focused on *ex vivo* removal of biofilms with promising outcomes, future work should consider the investigation of *in vivo* application and related biosafety of the hydrogel.

## Data availability statement

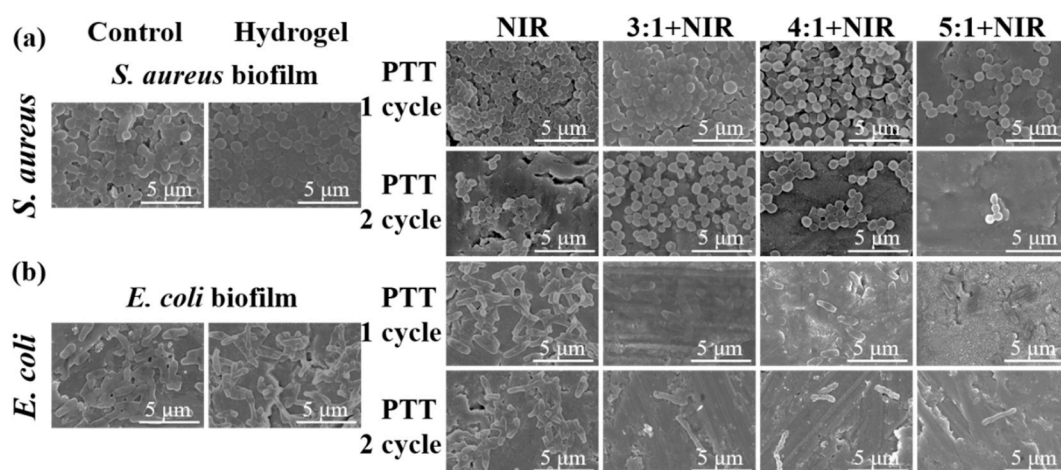All data to support the conclusions have been provided.



**Fig. 6.** SEM images of (a) *S. aureus* and (b) *E. coli* biofilms after no exposure (control), exposure to 5:1 hydrogel alone, exposure to light (2.0 mW/cm$^2$) alone, and simultaneous exposure to hydrogels (3:1, 4:1, and 5:1) and light (2.0 mW/cm$^2$) for 5 min.
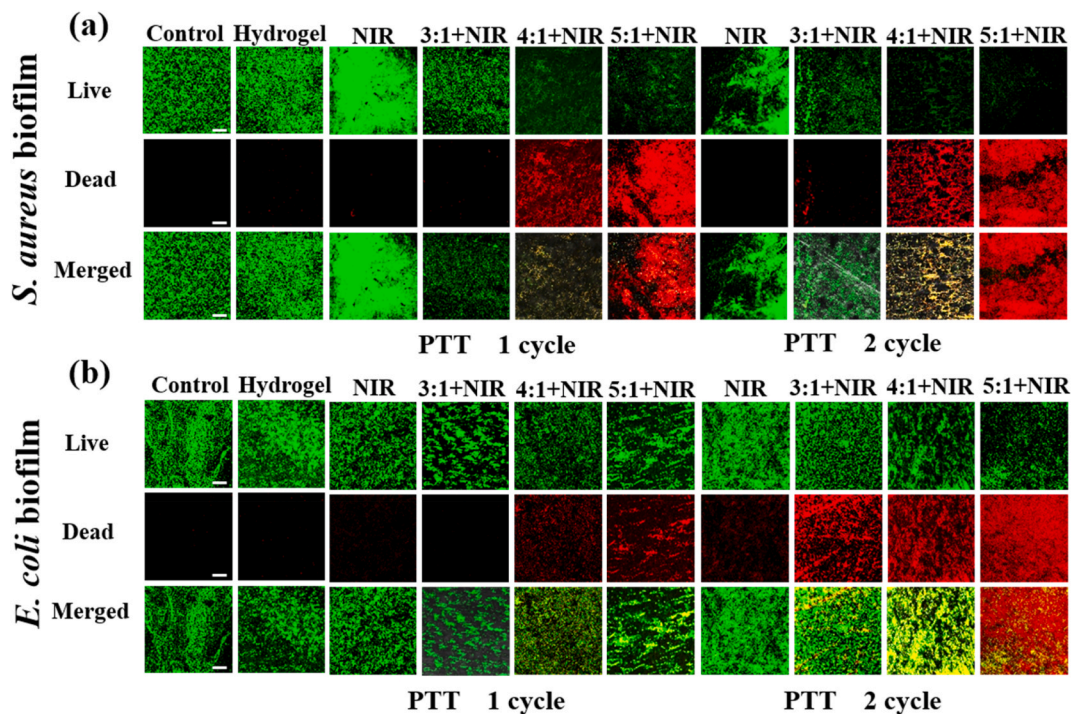
**Fig. 7.** Live/dead fluorescence staining of (a) *S. aureus* and (b) *E. coli* biofilms after no exposure (control), exposure to 5:1 hydrogel alone, exposure to light (2.0 mW/cm$^2$) alone, and simultaneous exposure to hydrogels (3:1, 4:1, and 5:1) and light (2.0 mW/cm$^2$) for 5 min.

## CRediT authorship contribution statement

**Yan Zhang:** Writing – original draft, Methodology, Investigation, Data curation, Conceptualization. **Hua Wei:** Methodology, Funding acquisition, Conceptualization. **Pingguang Zhu:** Writing – review & editing, Funding acquisition. **Xiaojuan Hao:** Writing – review & editing, Visualization, Validation, Methodology, Funding acquisition, Conceptualization. **Jing Chen:** Validation, Supervision, Funding acquisition, Data curation, Conceptualization. **Haina Zhang:** Writing – review & editing, Visualization, Validation, Funding acquisition.

## Declaration of competing interest

The authors declare that they have not known competing financial interests or personal relationships that could have appeared to influence the work reported in this paper.

## Acknowledgments

## Appendix A. Supplementary data

Supplementary data to this article can be found online at https://doi.org/10.1016/j.heliyon.2024.e34889.

## References

[1] H. Tian, J. Yan, W. Zhang, H. Li, S. Jiang, H. Qian, X. Chen, X. Dai, X. Wang, Cu-GA-coordination polymer nanozymes with triple enzymatic activity for wound disinfection and accelerated wound healing, Acta Biomater. 167 (2023) 449–462, https://doi.org/10.1016/j.actbio.2023.05.048.

[2] N.-Y.T. Nguyen, N. Grelling, C.L. Wetteland, R. Rosario, H. Liu, Antimicrobial activities and mechanisms of magnesium oxide nanoparticles (nMgO) against pathogenic bacteria, yeasts, and biofilms, Sci. Rep. 8 (2018) 16260, https://doi.org/10.1038/s41598-018-34567-5.

[3] S.I.C. Ricardo, I.I.L. Anjos, N. Monge, C.M.C. Faustino, I.A.C. Ribeiro, A glance at antimicrobial strategies to prevent catheter-associated medical infections, ACS Infect. Dis. 6 (2020) 3109–3130, https://doi.org/10.1021/acsinfecdis.0c00526.

[4] M. Riool, L. de Boer, V. Jaspers, C.M. van der Loos, W.J.B. van Wamel, G. Wu, P.H.S. Kwakman, S.A.J. Zaat, Staphylococcus epidermidis originating from titanium implants infects surrounding tissue and immune cells, Acta Biomater. 10 (2014) 5202–5212, https://doi.org/10.1016/j.actbio.2014.08.012.

[5] Y. Han, W. Zhao, Y. Zheng, H. Wang, Y. Sun, Y. Zhang, J. Luo, H. Zhang, Self-adhesive lubricated coating for enhanced bacterial resistance, Bioact. Mater. 6 (2021) 2535–2545, https://doi.org/10.1016/j.bioactmat.2021.01.028.

[6] E.A. Masters, B.F. Ricciardi, K.L.d.M. Bentley, T.F. Moriarty, E.M. Schwarz, G. Muthukrishnan, Skeletal infections: microbial pathogenesis, immunity and clinical management, Nat. Rev. Microbiol. 20 (2022) 385–400, https://doi.org/10.1038/s41579-022-00686-0.

[7] J.-B. Park, S.-H. Lee, N. Kim, S. Park, S.-H. Jin, B.-K. Choi, K.-K. Kim, Y. Ko, Instrumentation with ultrasonic scalers facilitates cleaning of the sandblasted and acid-etched titanium implants, J. Oral Implantol. 41 (2015) 419–428, https://doi.org/10.1563/AAID-JOI-D-13-00078.

[8] C.S. Tastepe, X. Lin, A. Werner, M. Donnet, D. Wismeijer, Y. Liu, Cleaning effect of osteoconductive powder abrasive treatment on explanted human implants and biofilm-coated titanium discs, Clinical and experimental dental research 4 (2018) 25–34, https://doi.org/10.1002/cre2.100.

[9] N. Vyas, R. Sammons, O. Addison, H. Dehghani, A. Walmsley, A quantitative method to measure biofilm removal efficiency from complex biomaterial surfaces using SEM and image analysis, Sci. Rep. 6 (2016) 32694, https://doi.org/10.1038/srep32694.

[10] M. Göltz, M. Koch, R. Detsch, M. Karl, A. Burkovski, S. Rosiwal, Influence of in-situ electrochemical oxidation on implant surface and colonizing microorganisms evaluated by scanning electron microscopy, Materials 12 (23) (2019), https://doi.org/10.3390/ma12233977.

[11] A.A. Al-Hashedi, M. Laurenti, M.-N. Abdallah, R.F. Albuquerque Jr., F. Tamimi, Electrochemical treatment of contaminated titanium surfaces in vitro: an approach for implant surface decontamination, ACS Biomater. Sci. Eng. 2 (2016) 1504–1518, https://doi.org/10.1021/acsbiomaterials.6b00265.

[12] E.C. Rodríguez-Merchán, D.J. Davidson, A.D. Liddle, Recent strategies to combat infections from biofilm-forming bacteria on orthopaedic implants, Int. J. Mol. Sci. 22 (2021) 10243, https://doi.org/10.3390/ijms221910243.

[13] C. Yang, Y. Luo, H. Lin, M. Ge, J. Shi, X. Zhang, Niobium carbide MXene augmented medical implant elicits bacterial infection elimination and tissue regeneration, ACS Nano 15 (2021) 1086–1099, https://doi.org/10.1021/acsnano.0c08045.

[14] J. Ouyang, A. Xie, J. Zhou, R. Liu, L. Wang, H. Liu, N. Kong, W. Tao, Minimally invasive nanomedicine: nanotechnology in photo-/ultrasound-/radiation-/magnetism-mediated therapy and imaging, Chem. Soc. Rev. 51 (2022) 4996–5041, https://doi.org/10.1039/D1CS01148K.

[15] W. Sun, F.-G. Wu, Two-dimensional materials for antimicrobial applications: graphene materials and beyond, Chem. Asian J. 13 (2018) 3378–3410, https://doi.org/10.1002/asia.201800851.

[16] J. Yin, Q. Han, J. Zhang, Y. Liu, X. Gan, K. Xie, L. Xie, Y. Deng, MXene-based hydrogels endow polyetheretherketone with effective osteogenicity and combined treatment of osteosarcoma and bacterial infection, ACS Appl. Mater. Interfaces 12 (2020) 45891–45903, https://doi.org/10.1021/acsami.0c14752.

[17] F. Wu, H. Zheng, W. Wang, Q. Wu, Q. Zhang, J. Guo, B. Pu, X. Shi, J. Li, X. Chen, W. Hong, Rapid eradication of antibiotic-resistant bacteria and biofilms by MXene and near-infrared light through photothermal ablation, Sci. China Mater. 64 (2021) 748–758, https://doi.org/10.1007/s40843-020-1451-7.

[18] C. Liu, P. Yang, J. Li, S. Cao, J. Shi, NIR/pH-responsive chitosan hydrogels containing Ti3C2/AuNRs with NIR-triggered photothermal effect, Carbohydr. Polym. 295 (2022) 119853, https://doi.org/10.1016/j.carbpol.2022.119853.

[19] X. He, S. Koo, E. Obeng, A. Sharma, J. Shen, J.S. Kim, Emerging 2D MXenes for antibacterial applications: current status, challenges, and prospects, Coord. Chem. Rev. 492 (2023) 215275, https://doi.org/10.1016/j.ccr.2023.215275.

[20] X. Luo, L. Zhu, Y.C. Wang, J. Li, J. Nie, Z.L. Wang, A flexible multifunctional triboelectric nanogenerator based on MXene/PVA hydrogel, Adv. Funct. Mater. 31 (2021) 2104928, https://doi.org/10.1002/adfm.202104928.

[21] F. Cheng, X. Yi, J. Dai, Z. Fan, J. He, Y. Huang, H. Li, Photothermal MXene@ Zn-MOF-decorated bacterial cellulose-based hydrogel wound dressing for infectious wound healing, Cell Reports Physical Science 4 (2023), https://doi.org/10.1016/j.xcrp.2023.101619.

[22] X. He, Y. Qian, C. Wu, J. Feng, X. Sun, Q. Zheng, X. Li, J. Shen, Entropy-mediated high-entropy MXenes nanotherapeutics: NIR-II-enhanced intrinsic oxidase mimic activity to combat methicillin-resistant Staphylococcus Aureus infection, Adv. Mater. 35 (2023) 2211432, https://doi.org/10.1002/adma.202211432.

[23] S. Iravani, R.S. Varma, MXene-based composites against antibiotic-resistant bacteria: current trends and future perspectives, RSC Adv. 13 (2023) 9665–9677, https://doi.org/10.1039/D3RA01276J.

[24] J. Ji, L. Zhao, Y. Shen, S. Liu, Y. Zhang, Covalent stabilization and functionalization of MXene via silylation reactions with improved surface properties, FlatChem 17 (2019) 100128, https://doi.org/10.1016/j.flatc.2019.100128.

[25] G. Zhang, T. Wang, Z. Xu, M. Liu, C. Shen, Q. Meng, Synthesis of amino-functionalized Ti3C2Tx MXene by alkalization-grafting modification for efficient lead adsorption, Chem. Commun. 56 (2020) 11283–11286, https://doi.org/10.1039/D0CC04265J.

[26] Z. Zhang, D. He, Z. Wang, S. Wu, T. Liu, Bimetallic palladium chromium nanoparticles anchored on amine-functionalized titanium carbides for remarkably catalytic dehydrogenation of formic acid at mild conditions, J. Catal. 410 (2022) 121–127, https://doi.org/10.1016/j.jcat.2022.04.021.

[27] B. Lü, Q. Gao, P. Li, J. Rao, Z. Lv, M. Shi, Y. Hu, X. Hao, G. Chen, M. Yin, F. Peng, Natural ultralong hemicelluloses phosphorescence, Cell Reports Physical Science 3 (2022) 101015, https://doi.org/10.1016/j.xcrp.2022.101015.

[28] Q. Li, Y. Niu, P. Xing, C. Wang, Bioactive polysaccharides from natural resources including Chinese medicinal herbs on tissue repair, Chin. Med. 13 (2018) 7, https://doi.org/10.1186/s13020-018-0166-0.

[29] C.K. Simi, T.E. Abraham, Transparent xyloglucan–chitosan complex hydrogels for different applications, Food Hydrocolloids 24 (2010) 72–80, https://doi.org/10.1016/j.foodhyd.2009.08.007.

[30] H. Wei, S. Yu, Y. Zhang, H. Zhang, Y. Ma, M. Xu, P. An, Y. Zhou, S. Halila, Y. Wei, Injectable chitosan/xyloglucan composite hydrogel with mechanical adaptivity and endogenous bioactivity for skin repair, Carbohydr. Polym. 313 (2023) 120904, https://doi.org/10.1016/j.carbpol.2023.120904.

[31] X. Li, L. Sun, P. Zhang, Y. Wang, Novel approaches to combat medical device-associated BioFilms, Coatings [Internet] 11 (3) (2021), https://doi.org/10.3390/coatings11030294.

[32] M. Canty, N. Luke-Marshall, A. Campagnari, M. Ehrensberger, Cathodic voltage-controlled electrical stimulation of titanium for prevention of methicillin-resistant Staphylococcus aureus and Acinetobacter baumannii biofilm infections, Acta Biomater. 48 (2017) 451–460, https://doi.org/10.1016/j.actbio.2016.11.056.

[33] S. Kumar, Y. Lei, N.H. Alshareef, M.A. Quevedo-Lopez, K.N. Salama, Biofunctionalized two-dimensional Ti3C2 MXenes for ultrasensitive detection of cancer biomarker, Biosens. Bioelectron. 121 (2018) 243–249, https://doi.org/10.1016/j.bios.2018.08.076.

[34] H. Riazi, M. Anayee, K. Hantanasirisakul, A.A. Shamsabadi, B. Anasori, Y. Gogotsi, M. Soroush, Surface modification of a MXene by an aminosilane coupling agent, Adv. Mater. Interfac. 7 (2020) 1902008, https://doi.org/10.1002/admi.201902008.

[35] R. Luo, W. Zhang, X. Hu, Y. Liang, J. Fu, M. Liu, F. Deng, Q.-Y. Cao, X. Zhang, Y. Wei, Preparation of sodium ligninsulfonate functionalized MXene using hexachlorocyclotriphosphazene as linkage and its adsorption applications, Appl. Surf. Sci. 602 (2022) 154197, https://doi.org/10.1016/j.apsusc.2022.154197.

[36] A.N. Kumar, K. Pal, Amine-functionalized stable Nb2CTx MXene toward room temperature ultrasensitive NO2 gas sensor, Materials Advances 3 (2022) 5151–5162, https://doi.org/10.1039/D2MA00301E.

[37] M. Rethinasabapathy, S.K. Hwang, S.-M. Kang, C. Roh, Y.S. Huh, Amino-functionalized POSS nanocage-intercalated titanium carbide (Ti3C2Tx) MXene stacks for efficient cesium and strontium radionuclide sequestration, J. Hazard Mater. 418 (2021) 126315, https://doi.org/10.1016/j.jhazmat.2021.126315.

[38] Q. Wu, N. Li, Y. Wang, Y. Xu, J. Wu, G. Jia, F. Ji, X. Fang, F. Chen, X. Cui, Ultrasensitive and selective determination of carcinoembryonic antigen using multifunctional ultrathin amino-functionalized Ti3C2-MXene nanosheets, Anal. Chem. 92 (2020) 3354–3360, https://doi.org/10.1021/acs.analchem.9b05372.

[39] C. Qu, S. Li, Y. Zhang, T. Wang, Q. Wang, S. Chen, Surface modification of Ti3C2-MXene with polydopamine and amino silane for high performance nitrile butadiene rubber composites, Tribol. Int. 163 (2021) 107150, https://doi.org/10.1016/j.triboint.2021.107150.

[40] A. Kong, Y. Sun, M. Peng, H. Gu, Y. Fu, J. Zhang, W. Li, Amino-functionalized MXenes for efficient removal of Cr(VI), Colloids Surf. A Physicochem. Eng. Asp. 617 (2021) 126388, https://doi.org/10.1016/j.colsurfa.2021.126388.

[41] M.-C. Brochier Salon, P.-A. Bayle, M. Abdelmouleh, S. Boufi, M.N. Belgacem, Kinetics of hydrolysis and self condensation reactions of silanes by NMR spectroscopy, Colloids Surf. A Physicochem. Eng. Asp. 312 (2008) 83–91, https://doi.org/10.1016/j.colsurfa.2007.06.028.

[42] A.I. Van Den Bulcke, B. Bogdanov, N. De Rooze, E.H. Schacht, M. Cornelissen, H. Berghmans, Structural and rheological properties of methacrylamide modified gelatin hydrogels, Biomacromolecules 1 (2000) 31–38, https://doi.org/10.1021/bm990017d.

[43] M. Han, Y. Liu, R. Huang, D. Sun, W. Zhang, J. Jiang, Characterization of structure and solution properties of tamarind seed polysaccharide extracted at different temperatures, J. Biobased Mater. Bioenergy 12 (2018) 175–183, https://doi.org/10.1166/jbmb.2018.1760.

[44] M. Han, Y. Liu, F. Zhang, D. Sun, J. Jiang, Effect of galactose side-chain on the self-assembly of xyloglucan macromolecule, Carbohydr. Polym. 246 (2020) 116577, https://doi.org/10.1016/j.carbpol.2020.116577.

[45] H. Herrada-Manchón, M.A. Fernández, E. Aguilar, Essential guide to hydrogel rheology in extrusion 3D printing: how to measure it and why it matters? Gels 9 (7) (2023) https://doi.org/10.3390/gels9070517 [Internet].

[46] S. Anjum, P. Gurave, M.V. Badiger, A. Torris, N. Tiwari, B. Gupta, Design and development of trivalent aluminum ions induced self-healing polyacrylic acid novel hydrogels, Polymer 126 (2017) 196–205, https://doi.org/10.1016/j.polymer.2017.08.045.

[47] Y.-Y. Peng, Q. Cheng, M. Wu, W. Wang, J. Zhao, D. Diaz-Dussan, M. McKay, H. Zeng, S. Ummartyotin, R. Narain, Highly stretchable, self-healing, injectable and pH responsive hydrogel from multiple hydrogen bonding and boron-carbohydrate interactions, Gels [Internet] 9 (9) (2023), https://doi.org/10.3390/gels9090709.

[48] C. Huang, Q. Luo, Q. Miao, Z. He, P. Fan, Y. Chen, Q. Zhang, X. He, L. Li, X. Liu, MXene-based double-network organohydrogel with excellent stretchability, high toughness, anti-drying and wide sensing linearity for strain sensor, Polymer 253 (2022) 124993, https://doi.org/10.1016/j.polymer.2022.124993.

[49] S. Nam, D. Mooney, Polymeric tissue adhesives, Chem. Rev. 121 (2021) 11336–11384, https://doi.org/10.1021/acs.chemrev.0c00798.

[50] A. Rosenkranz, G. Perini, J.Y. Aguilar-Hurtado, D.F. Zambrano, B. Wang, B. Niccolini, P.C. Henriques, E. Rosa, F. De Maio, G. Delogu, M. De Spirito, V. Palmieri, M. Papi, Laser-Mediated antibacterial effects of few- and multi-layer $Ti_3C_2T_x$ MXenes, Appl. Surf. Sci. 567 (2021) 150795, https://doi.org/10.1016/j.apsusc.2021.150795.

[51] L. Thieme, A. Hartung, K. Tramm, M. Klinger-Strobel, K.D. Jandt, O. Makarewicz, M.W. Pletz, MBEC versus MBIC: the lack of differentiation between biofilm reducing and inhibitory effects as a current problem in biofilm methodology, Biol. Proced. Online 21 (2019) 18, https://doi.org/10.1186/s12575-019-0106-0.